Extending the 1-D Hovel Model for Coherent and Incoherent Back Reflections in Homojunction Solar Cells

Matthew P. Lumb, Christopher G. Bailey, Jessica G. J. Adams, Glen Hillier, Francis Tuminello, Victor C. Elarde, and Robert J. Walters

***Abstract*— In this paper we extend the analytical drift-diffusion model, or Hovel model, to model the electrical characteristics of solar cells incorporating a back mirror. We use a compact summation approach to derive modified optical generation functions in Homojunction solar cells, considering both coherent and incoherent reflections from the back reflector. These modified generation functions are then used to derive analytical formulae for the current–voltage characteristics of mirrored solar cells. We simulate the quantum efficiency of a simple GaAs np diode with a planar gold back reflector, and compare the results with the standard Hovel model using a generation function given by the Beer–Lambert law. Finally, we use the model to simulate the performance of a real GaAs solar cell device fabricated using an epitaxial-lift-off procedure, demonstrating excellent agreement between the simulated and measured characteristics.**

***Index Terms*— Photovoltaic cells, reflection, semiconductor device modeling.**

I. Introduction

THE ANALYTICAL solution to the drift-diffusion problem is an efficient and powerful tool to predict the performance of solar cells. While numerical solvers generally allow greater flexibility in the specific device structures that can be modeled, solar cells can be modeled analytically without the need for numerical methods. However, in order for the analytical solution to be accurate, the solar cells must satisfy the requirements for the specific boundary conditions applied to the charge-transport equations, which allow the mathematical separation of the field-bearing and quasi-neutral regions (QNR) of the solar cell. For instance, uniform compositions and doping profiles in the emitter and base regions are required. Furthermore, the doping levels in the emitter and base regions should be low enough to for Boltzmann statistics to be applied, and the solution requires the system to be in the low-injection regime. In this regime, the density of photogenerated carriers is smaller than the equilibrium majority carrier density in the QNRs. This results in linear minority carrier recombination rates, which allow the light and dark components of the current terms to be separated, meaning that only minority carriers are required in the transport equations for the QNRs.

This analytical approach is often termed the Hovel, or Hovel–Woodall model, after the researchers who made the early progress in developing the analytical approach in a series of landmark publications [1], [2]. Although widely accepted, an obvious drawback is in the simplicity of the generation function used. The photon flux in the solar cell medium is assumed to follow a Beer–Lambert type function, which is a good assumption for materials with no highly reflecting interfaces. However, the use of reflecting surfaces to boost the photocurrent production of current state of the art solar cells is now a commonplace technology. Although work has been done to calculate the generation functions of thin-film solar cells with a variety of back reflection properties, such as planar mirrors, Lambertian reflectors, diffraction gratings and textured coatings [3]–[8], so far no detailed derivation of the photocurrent production with the modified generation function and realistic minority carrier transport properties has been attempted. Thus, only numerical approaches are capable of fully accounting for the modified generation function in the structure [9]–[13].

Calculating the photon flux in a 1-D multilayer is straightforward using a transfer matrix method [14], but the problem cannot be easily integrated with the Hovel model as the expanded expressions describing the position dependent flux become prohibitively complicated for relatively few layers. In this paper, we use a compact summation method based on the simple case of a homojunction with nonzero front and rear reflectivity to produce a full solution to the analytical model, examining both coherent and incoherent reflections [15]. This is limited in scope, as many thin-film designs employ heterostructures and/or textured reflecting surfaces for light-trapping, but for a basic homojunction incorporating a planar back reflector the approach is suitable, provided the conditions of the Hovel model are met. Extending the approach to more complex geometries, such as textured layers and Lambertian reflectors, will be the subject of further study.

II. No Back Reflection

In this paper we adopt a similar nomenclature for the thicknesses of the layers in the solar cell as Fonash [16],

Manuscript received January 30, 2013; revised March 5, 2013; accepted March 7, 2013. Date of publication March 11, 2013; date of current version April 5, 2013. This work was supported by the Office of Naval Research.

M. P. Lumb is with the Naval Research Laboratory, Washington, DC 20375 USA, and also with George Washington University, Washington, DC 20037 USA (e-mail: matthew.lumb.ctr.uk@nrl.navy.mil).

C. G. Bailey and R. J. Walters are with the Naval Research Laboratory, Washington, DC 20375 USA (e-mail: chris.bailey.ctr@nrl.navy.mil; robert.walters@nrl.navy.mil).

J. G. J. Adams, G. Hillier, F. Tuminello, and V. C. Elarde are with MicroLink Devices, Inc., Niles, IL 60714 USA (e-mail: jadams@mldevices.com; GHillier@mldevices.com; ftuminello@mldevices.com; velarde@mldevices.com).

Digital Object Identifier 10.1109/JQE.2013.2252148

0018-9197/$31.00 © 2013 IEEE

$$J_p = q\int F_0(\lambda)\left\{\frac{L_pF_1(\lambda)+\frac{S_pL_p}{D_p}F_2(\lambda)-F_3(\lambda)\left(\sinh\frac{D_1}{L_p}+\frac{S_pL_p}{D_p}\cosh\frac{d_1}{L_p}\right)}{\left(\cosh\frac{d_1}{L_p}+\frac{S_pL_p}{D_p}\sinh\frac{d_1}{L_p}\right)}-L_pF_4(\lambda)\right\}d\lambda$$
$$+\frac{qD_pp_0\left(e^{qV/kT}-1\right)}{L_p}\left\{\frac{\sinh\frac{d_1}{L_p}+\frac{S_pL_p}{D_p}\cosh\frac{d_1}{L_p}}{\cosh\frac{d_1}{L_p}+\frac{S_pL_p}{D_p}\sinh\frac{d_1}{L_p}}\right\}. \quad (3)$$

$$j_p(\lambda) = qF_0(\lambda)\left\{\frac{L_pF_1(\lambda)+\frac{S_pL_p}{D_p}F_2(\lambda)-F_3(\lambda)\left(\sinh\frac{d_1}{L_p}+\frac{S_pL_p}{D_p}\cosh\frac{d_1}{L_p}\right)}{\left(\cosh\frac{d_1}{L_p}+\frac{S_pL_p}{D_p}\sinh\frac{d_1}{L_p}\right)}-L_pF_4(\lambda)\right\}. \quad (9)$$

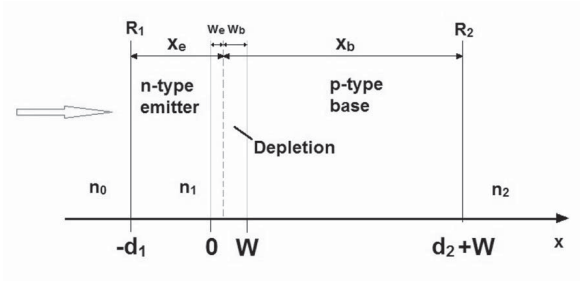

Fig. 1. Schematic diagram of the layer structure and naming scheme for the analytical solar cell model.

and Fig. 1 shows the layer structure for the cell and the naming scheme. The emitter and base thicknesses are denoted X_e and X_b respectively and the depletion widths in each layer are w_e and w_b for the emitter and base respectively. The thickness of the quasi-neutral region in the emitter is $d_1 = X_e - w_e$ and the thickness of the QNR in the base is $d_2 = X_b - w_b$. The total depletion width of the structure is given by $W = w_e + w_b$. The reflectivity of the front and rear surfaces of the solar cell are denoted R_1 and R_2 respectively and the total thickness of the solar cell is the sum of the n-type QNR, the depletion region and the p-type QNR, $P = d_1 + W + d_2$. The emitter and base of the solar cell are assumed to be the same material and, for simplicity, the cell is assumed to not contain a window or back surface field layer.

Within the n-type QNR for the example in Fig. 1, the minority hole density, p, as a function of position satisfies

$$\frac{d^2p}{dx^2}-\frac{p-p_0}{L_p^2}+\int\frac{\alpha\varphi(x)}{D_p}d\lambda = 0 \quad (1)$$

where p_0 represents the minority carrier (hole) density under equilibrium conditions and L_p and D_p represent the minority carrier diffusion length and diffusivity, respectively. The absorption coefficient of the material is given by α and $\varphi(x)$ describes the photon flux as a function of depth in the cell. For the case of no back reflection, $\varphi(x)$ is described by the Beer-Lambert law as follows

$$\varphi(x) = (1-R_1)\varphi_0e^{-\alpha(x+d_1)}. \quad (2)$$

Here R_1 is the reflectance of the front surface of the solar cell and φ_0 is the flux incident on the solar cell. The expression for the current density can be derived by solving (1) and applying the boundary conditions arising from the requirement of current continuity. The hole current density is evaluated at $x = 0$, the plane just outside the space charge region in the n-type layer. The hole current density may be evaluated at this point provided the holes remain a minority carrier in the emitter, even under illumination, also provided the region $x = 0$ is space charge neutral and the lifetime of the minority carriers is much longer than the dielectric relaxation time in the material. A detailed discussion of the specific assumptions used and a full derivation can be found in Fonash [16], and only the result is presented here. To simplify the notation, five wavelength dependent coefficients, F_{0-4}, are defined, and the emitter current density is given in (3), shown at the top of the page.

The coefficients F_{0-4} are

$$F_0(\lambda) = \frac{L_p(1-R_1)\alpha\varphi_0}{\left(1-\alpha^2L_p^2\right)} \quad (4)$$
$$F_1(\lambda) = \alpha \quad (5)$$
$$F_2(\lambda) = 1 \quad (6)$$
$$F_3(\lambda) = e^{-\alpha d_1} \quad (7)$$
$$F_4(\lambda) = \alpha e^{-\alpha d_1}. \quad (8)$$

The external quantum efficiency (EQE) can now be derived by evaluating the spectral photocurrent, denoted by a lowercase j, from excitation by a monochromatic light source and for $V = 0$, leading to the well-known result from Hovel given in (9), shown at the top of the page.

Similarly, in the p-type QNR, the minority electron density as a function of position satisfies

$$\frac{d^2n}{dx^2}-\frac{n-n_0}{L_n^2}+\int\frac{\alpha\varphi(x)}{D_n}d\lambda = 0 \quad (10)$$

where now n_0 is the equilibrium concentration of minority electrons, L_n and D_n are the minority electron diffusion length and diffusivity, respectively. The electron current density is evaluated at $x = W$, the plane just outside the space charge region in the p-type region and subject to the same assumptions as the hole current density. As before, the current density can be shown to be given by (11), shown at the top of next page.

The coefficients are

$$F_5(\lambda) = \frac{L_n(1-R_1)\alpha\varphi_0}{\left(1-\alpha^2L_n^2\right)} \quad (12)$$
$$F_6(\lambda) = \alpha e^{-\alpha d_2} \quad (13)$$

$$J_n = qe^{-\alpha(W+d_1)} \int F_5(\lambda) \left\{ \frac{L_n F_6(\lambda) - \frac{S_n L_n}{D_n} F_7(\lambda) + F_8(\lambda) \left(\sinh \frac{d_2}{L_n} + \frac{S_n L_n}{D_n} \cosh \frac{d_2}{L_n} \right)}{\left(\cosh \frac{d_2}{L_n} + \frac{S_n L_n}{D_n} \sinh \frac{d_2}{L_n} \right)} - L_n F_9(\lambda) \right\} d\lambda + \frac{q D_n n_0 \left(e^{qV/kT} - 1 \right)}{L_n} \left\{ \frac{\sinh \frac{d_2}{L_n} + \frac{S_n L_n}{D_n} \cosh \frac{d_2}{L_n}}{\cosh \frac{d_2}{L_n} + \frac{S_n L_n}{D_n} \sinh \frac{d_2}{L_n}} \right\}. \quad (11)$$

$$j_n(\lambda) = qe^{-\alpha(W+d_1)} F_5(\lambda) \left\{ \frac{L_n F_6(\lambda) - \frac{S_n L_n}{D_n} F_7(\lambda) + F_8(\lambda) \left(\sinh \frac{d_2}{L_n} + \frac{S_n L_n}{D_n} \cosh \frac{d_2}{L_n} \right)}{\left(\cosh \frac{d_2}{L_n} + \frac{S_n L_n}{D_n} \sinh \frac{d_2}{L_n} \right)} - L_n F_9(\lambda) \right\}. \quad (17)$$

$$F_7(\lambda) = e^{-\alpha d_2} \quad (14)$$

$$F_8(\lambda) = 1 \quad (15)$$

$$F_9(\lambda) = \alpha. \quad (16)$$

The spectral photocurrent arising from excitation by a monochromatic light source and for $V = 0$ is therefore in (17), shown at the top of the page.

Finally, in the depletion region, the spectral photocurrent is equal to the integral of the generation function

$$j_d(\lambda) = q(1 - R_1)\varphi_0 e^{-\alpha d_1} \left(1 - e^{-\alpha W} \right). \quad (18)$$

III. Incoherent Back Reflection

In the case of incoherent back reflection, the intensities of the multiple reflected beams add at all positions in the cell. The flux at position x can be found from the sum of all the reflected beams

$$\varphi(x) = (1 - R_1)\varphi_0 \times \Big[e^{-\alpha(x+d_1)} + e^{-2\alpha P} R_2 e^{\alpha(x+d_1)} + e^{-2\alpha P} R_1 R_2 e^{-\alpha(x+d_1)} + e^{-4\alpha P} R_1 R_2^2 e^{\alpha(x+d_1)} + e^{-4\alpha P} R_1^2 R_2^2 e^{-\alpha(x+d_1)} + \cdots \Big]. \quad (19)$$

Recognizing this series as a geometric progression, the sum of an infinite number of reflected beams is given by

$$\varphi(x) = (1 - R_1) \frac{\varphi_0 \left(e^{-\alpha(x+d_1)} + e^{-2\alpha P} R_2 e^{\alpha(x+d_1)} \right)}{1 - R_1 R_2 e^{-2\alpha P}}. \quad (20)$$

By solving (1) with the new function for the photon flux, it is possible to derive a new set of F coefficients for the n-type emitter region, which can be substituted into (3)

$$F_0(\lambda) = \frac{L_p(1 - R_1)\alpha\varphi_0}{\left(1 - \alpha^2 L_p^2 \right)\left(1 - R_1 R_2 e^{-2\alpha P} \right)} \quad (21)$$

$$F_1(\lambda) = \left(\alpha - \alpha e^{-2\alpha P} R_2 \right) \quad (22)$$

$$F_2(\lambda) = \left(1 + e^{-2\alpha P} R_2 \right) \quad (23)$$

$$F_3(\lambda) = \left(e^{-\alpha d_1} + e^{-2\alpha P} R_2 e^{\alpha d_1} \right) \quad (24)$$

$$F_4(\lambda) = \alpha \left(e^{-\alpha d_1} - e^{-2\alpha P} R_2 e^{\alpha d_1} \right). \quad (25)$$

In the base region the F coefficients are

$$F_5(\lambda) = \frac{L_n(1 - R_1)\alpha\varphi_0}{\left(1 - \alpha^2 L_n^2 \right)\left(1 - R_1 R_2 e^{-2\alpha P} \right)} \quad (26)$$

$$F_6(\lambda) = \alpha e^{-\alpha d_2}(1 - R_2) \quad (27)$$

$$F_7(\lambda) = e^{-\alpha d_2}(1 + R_2) \quad (28)$$

$$F_8(\lambda) = \left(1 + R_2 e^{-2\alpha d_2} \right) \quad (29)$$

$$F_9(\lambda) = \alpha \left(1 - R_2 e^{-2\alpha d_2} \right). \quad (30)$$

As in the simple Beer–Lambert case, the depletion region spectral photocurrent is equal to the integral of the generation function

$$j_d(\lambda) = \frac{q(1 - R_1)\varphi_0 e^{-\alpha d_1}}{\left(1 - R_1 R_2 e^{-2\alpha P} \right)} \times \left(1 - e^{-\alpha W} + R_2 e^{2\alpha(d_1 - P)} \left(e^{\alpha W} - 1 \right) \right). \quad (31)$$

IV. Coherent Back Reflection

In the case of coherent back reflection, the phase of the multiple reflected beams is conserved and thus the forward and reverse propagating fields interfere. For an electric field impinging on the top surface of the solar cell with amplitude E_0, the field amplitude after successive reflections in the solar cell is shown schematically in Fig. 2.

The electric field at position x is found from the following series:

$$E(x) = t_1 E_0^+ \Big[e^{-i\delta(x+d_1)} + e^{-2i\delta P} r_2 e^{i\delta(x+d_1)} - e^{-2i\delta P} r_1 r_2 e^{-i\delta(x+d_1)} - e^{-4i\delta P} r_1 r_2^2 e^{i\delta(x+d_1)} + e^{-4i\delta P} r_1^2 r_2^2 e^{-i\delta(x+d_1)} + \cdots \Big]. \quad (32)$$

In this notation, r_1 and r_2 are the Fresnel reflection amplitude of the front and rear surfaces respectively and the phase factor δ is given by

$$\delta = \frac{2\pi \widetilde{\mathbf{n}}}{\lambda}. \quad (33)$$

where the complex refractive index of the solar cell material is $\widetilde{\mathbf{n}} = n - ik$. Note that the Fresnel reflection amplitude from material 1 to material 0 is $-r_1$, where r_1 was defined as the reflection amplitude from material 0 to material 1

$$E(x) = \frac{t_1 E_0^+ \left(e^{-i\delta(x+d_1)} + e^{-2i\delta P} r_2 e^{i\delta(x+d_1)} \right)}{1 + r_1 r_2 e^{-2i\delta P}}. \quad (34)$$

$$\varphi(x) = (1-R_1)\frac{\varphi_0\left(e^{-\alpha(x+d_1)} + e^{\alpha(x+d_1)}e^{-2\alpha P}R_2 + e^{-\alpha P}\left[r_2 e^{i\frac{4\pi}{\lambda}n(x+d_1-P)} + r_2^* e^{-i\frac{4\pi}{\lambda}n(x+d_1-P)}\right]\right)}{e^{-\alpha P}\left[r_1 r_2 e^{-i\frac{4\pi}{\lambda}nP} + r_1^* r_2^* e^{i\frac{4\pi}{\lambda}nP}\right] + e^{-2\alpha P}R_1R_2 + 1} \tag{35}$$

$$F_0(\lambda) = \frac{L_p(1-R_1)\alpha\varphi_0}{\left(e^{-\alpha P}\left[r_1 r_2 e^{-i\frac{4\pi}{\lambda}nP} + r_1^* r_2^* e^{i\frac{4\pi}{\lambda}nP}\right] + e^{-2\alpha P}R_1R_2 + 1\right)} \tag{36}$$

$$F_1(\lambda) = \left\{\frac{\left(\alpha - \alpha e^{-2\alpha P}R_2\right)}{\left(1-\alpha^2 L_p^2\right)} - e^{-\alpha P}\frac{\left(i\frac{4\pi n}{\lambda}r_2 e^{-i\frac{4\pi n}{\lambda}P} - i\frac{4\pi n}{\lambda}r_2^* e^{i\frac{4\pi n}{\lambda}P}\right)}{\left(1+L_p^2\left(\frac{4\pi n}{\lambda}\right)^2\right)}\right\} \tag{37}$$

$$F_2(\lambda) = \left\{\frac{\left(1+e^{-2\alpha P}R_2\right)}{\left(1-\alpha^2 L_p^2\right)} + e^{-\alpha P}\frac{\left(r_2 e^{-i\frac{4\pi n}{\lambda}P} + r_2^* e^{i\frac{4\pi n}{\lambda}P}\right)}{\left(1+L_p^2\left(\frac{4\pi n}{\lambda}\right)^2\right)}\right\} \tag{38}$$

$$F_3(\lambda) = \left\{\frac{\left(e^{-\alpha d_1} + e^{-2\alpha P}R_2 e^{\alpha d_1}\right)}{\left(1-\alpha^2 L_p^2\right)} + e^{-\alpha P}\frac{\left(r_2 e^{i\frac{4\pi n}{\lambda}(d_1-P)} + r_2^* e^{-i\frac{4\pi n}{\lambda}(d_1-P)}\right)}{\left(1+L_p^2\left(\frac{4\pi n}{\lambda}\right)^2\right)}\right\} \tag{39}$$

$$F_4(\lambda) = \left\{\frac{\alpha\left(e^{-\alpha d_1} - e^{-2\alpha P}R_2 e^{\alpha d_1}\right)}{\left(1-\alpha^2 L_p^2\right)} - e^{-\alpha P}\frac{\left(i\frac{4\pi n}{\lambda}r_2 e^{i\frac{4\pi n}{\lambda}(d_1-P)} - i\frac{4\pi n}{\lambda}r_2^* e^{-i\frac{4\pi n}{\lambda}(d_1-P)}\right)}{\left(1+L_p^2\left(\frac{4\pi n}{\lambda}\right)^2\right)}\right\}. \tag{40}$$

$$F_5(\lambda) = \frac{L_n(1-R_1)\alpha\varphi_0}{\left(e^{-\alpha P}\left[r_1 r_2 e^{-i\frac{4\pi}{\lambda}nP} + r_1^* r_2^* e^{i\frac{4\pi}{\lambda}nP}\right] + e^{-2\alpha P}R_1R_2 + 1\right)} \tag{41}$$

$$F_6(\lambda) = \left\{\frac{\alpha e^{-\alpha d_2}(1-R_2)}{\left(1-\alpha^2 L_n^2\right)} - e^{-\alpha d_2}\frac{\left(i\frac{4\pi n}{\lambda}r_2 - i\frac{4\pi n}{\lambda}r_2^*\right)}{\left(1+L_n^2\left(\frac{4\pi n}{\lambda}\right)^2\right)}\right\} \tag{42}$$

$$F_7(\lambda) = \left\{\frac{e^{-\alpha d_2}(1+R_2)}{\left(1-\alpha^2 L_n^2\right)} + e^{-\alpha d_2}\frac{\left(r_2 + r_2^*\right)}{\left(1+L_n^2\left(\frac{4\pi n}{\lambda}\right)^2\right)}\right\} \tag{43}$$

$$F_8(\lambda) = \left\{\frac{\left(1+R_2 e^{-2\alpha d_2}\right)}{\left(1-\alpha^2 L_n^2\right)} + e^{-\alpha d_2}\frac{\left(r_2 e^{-i\frac{4\pi n}{\lambda}d_2} + r_2^* e^{i\frac{4\pi n}{\lambda}d_2}\right)}{\left(1+L_n^2\left(\frac{4\pi n}{\lambda}\right)^2\right)}\right\} \tag{44}$$

$$F_9(\lambda) = \left\{\frac{\alpha\left(1-R_2 e^{-2\alpha d_2}\right)}{\left(1-\alpha^2 L_n^2\right)} - e^{-\alpha d_2}\frac{\left(i\frac{4\pi n}{\lambda}r_2 e^{-i\frac{4\pi n}{\lambda}d_2} - i\frac{4\pi n}{\lambda}r_2^* e^{i\frac{4\pi n}{\lambda}d_2}\right)}{\left(1+L_n^2\left(\frac{4\pi n}{\lambda}\right)^2\right)}\right\}. \tag{45}$$

The photon flux in the structure relative to the flux in air is in the same ratio as the intensity of the field, proportional to $E(x)E(x)^*$, and therefore given in (35), shown at the top of the page, where we have used the fact that $\alpha = 4\pi k/\lambda$. The coefficients F_{0-4} for the coherent back reflector case are given in (36)–(40), shown at the top of the page. The base region is given in (41)–(45), shown at the top of the page. As in the other cases, within the depletion region, the spectral photocurrent is equal to the integral of the generation function, resulting in

$$\begin{aligned} j_d(\lambda) &= \frac{q(1-R_1)\varphi_0}{e^{-\alpha P}\left[r_1 r_2 e^{-i\frac{4\pi}{\lambda}nP} + r_1^* r_2^* e^{i\frac{4\pi}{\lambda}nP}\right] + e^{-2\alpha P}R_1R_2 + 1} \\ &\times \left[e^{-\alpha d_1}\left(1 - e^{-\alpha W} + R_2 e^{2\alpha(d_1-P)}\left(e^{\alpha W} - 1\right)\right)\right. \\ &\quad + i\frac{\alpha\lambda}{4\pi n}e^{-\alpha P}\left(r_2^*\left(e^{-i\frac{4\pi n}{\lambda}d_2} - e^{-i\frac{4\pi n}{\lambda}(d_1-P)}\right)\right. \\ &\quad \left.\left. - r_2\left(e^{i\frac{4\pi n}{\lambda}d_2} - e^{i\frac{4\pi n}{\lambda}(d_1-P)}\right)\right)\right]. \end{aligned} \tag{46}$$

V. Results

Using the derived relations for the photo current of a solar cell, we simulated a GaAs np diode structure with an Au back reflector. The GaAs diode had a 100 nm emitter with n-type doping of 5.0×10^{17} cm^{-3} and a 1200 nm base with p-type doping of 5.0×10^{16} cm^{-3}. The emitter region of III–V solar cells typically have doping levels in the 10^{17}–10^{19} cm^{-3} range and are significantly thinner than the base region. The optimum doping level depends on the specific minority carrier mobility and lifetime properties of the emitter material. The validity of the model is affected if the material is degenerately doped as the equation are based on Boltzmann statistics, but the model also requires that the emitter doping is sufficiently high to guarantee the emitter depletion width is thinner than the total emitter thickness. The base region of the solar cell is typically

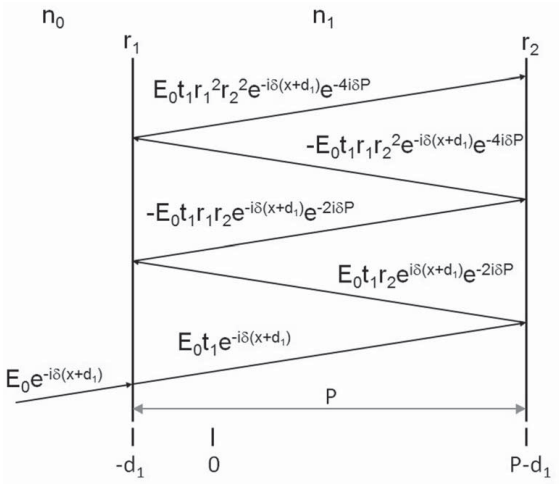

Fig. 2. Simplified view of the multiple coherent reflections in the solar cell. For illustrative purposes the reflections are shown at oblique incidence but the field amplitudes are derived for normal incidence.

thicker than the emitter region to absorb sufficient light. To ensure efficient carrier collection, the doping in the base region is usually lower than the emitter, with values typically in the 10^{16}–10^{18} cm^{-3} range, which can be optimized to improve the minority carrier diffusion length.

In this simulation, the optical constants of the GaAs were taken from Adachi [17]. The low-field carrier mobilities in GaAs were calculated using the empirical electron and hole mobility parameters taken from [18]. The minority electron and hole mobilities were calculated under the assumption that they take the majority electron and hole mobility values for any given doping concentration.

The radiative lifetime of minority carriers in a given layer is given by $\tau_r = (B_{\mathrm{rad}}N)^{-1}$, were B_{rad} is the bimolecular recombination coefficient, or B-coefficient, which was calculated using the equation given by Hall [19] and N is the doping concentration in the layer. The calculated B-coefficient of 2.86×10^{-10} $\mathrm{cm}^3\mathrm{s}^{-1}$ is in agreement to a recent study of n-type GaAs [20], which suggested a value of 1.8–3.5×10^{-10} cm^3/s depending on the doping concentration. Any carrier concentration dependence in B_{rad} was neglected in this model however. The overall minority carrier lifetime contains both radiative and nonradiative components, and a Shockley–Read–Hall lifetime of 20 ns was defined for electrons and holes in both the emitter and base regions. The overall minority carrier lifetime is then

$$\frac{1}{\tau} = \frac{1}{\tau_r} + \frac{1}{\tau_{\mathrm{SRH}}}. \tag{47}$$

Note that in our model, the B-coefficient is assumed to be independent of the reflectivity of the back surface. In reality, the modification to the spatial profile of the radiative emission can lead to a suppression of the B-coefficient, so called photon-recycling, which in situations where τ_{SRH} is long in comparison to τ_r could significantly modify the minority carrier lifetime. This has been observed solar cells incorporating multi quantum wells where the recombination at high forward bias is dominated by radiative recombination in the wells, and the presence of a back reflector leads to a suppression of this dark current contribution [21]. In this model we are working under the assumption that the modification to the B-coefficient can be neglected, and therefore neglecting the suppression of the dark current of the solar cell through photon recycling. In this case, the mechanism for improving the solar cell performance in the presence of a back-reflector is the improved photocurrent generation due to the multiple passes of light through the absorber layers. In the case of solar cells with very long nonradiative lifetimes and which are dominated by radiative recombination, this approximation may need to be revised.

The dark current in the QNRs was calculated using (3) and (11) with no generation. In the depletion region the dark current was assumed to be dominated by Shockley–Read–Hall recombination and calculated numerically using the following equation [22], assuming mid-gap trap levels

$$J_{\mathrm{SRH}} = -q \int_0^W \frac{np - n_i^2}{\tau_{\mathrm{SRH},n}\,(p + p_t) + \tau_{\mathrm{SRH},p}\,(n + n_t)} dx. \tag{48}$$

Here n_i is the intrinsic carrier density and n_t and p_t are the trap level densities. The position dependent carrier concentrations were calculated by computing the electrostatic potential in the emitter and base depletion regions, found by solving Poisson's equation with appropriate boundary conditions [23]. The electrostatic potential and the quasi-Fermi levels for electrons and holes were then used to compute n and p, assuming Boltzmann statistics. All band parameters used in the calculation of the solar cell IV characteristics were taken from the review article by Vurgaftman *et al.* [24], and interface recombination velocities at the front and rear surfaces of the solar cell were set to 5.0×10^5 cm/s. Fig. 3 shows the external quantum efficiency curves for solar cells with a coherent, incoherent and no back reflector. The long wavelength improvement to EQE is clearly visible, with pronounced fringes in the coherent case due to the interference of the forward and reverse propagating fields in the structure. The short circuit current densities (J_{sc}) for the three solar cells, calculated under illumination by the AM0 spectrum, are shown on the Fig. 3. The coherent and incoherent back reflectors produce similar enhancements to J_{sc} over the device without a back reflector, producing approximately 5–6% more photocurrent.

The photon flux as a function of depth in the solar cell relative to the incident photon flux is shown for 500, 650, and 800 nm light in Fig. 4 for no back reflection, incoherent back reflection and coherent back reflection. At short wavelengths, where the GaAs is strongly absorbing, the fringes in the coherent reflection case are suppressed due to the strong attenuation of the forward and reverse propagating fields. This is demonstrated by the 500 nm curves, where the generation profiles in the structure are identical for the three back reflector conditions. At 650 nm however, the generation profiles begin to deviate from the Beer–Lambert behavior as the absorption in the cavity becomes weaker and multiple reflections become stronger. At 800 nm the absorption is weak enough that the penetration depth of the light is much longer than the total thickness of the structure, so the back reflecting structures demonstrate an enhanced generation function. Also,

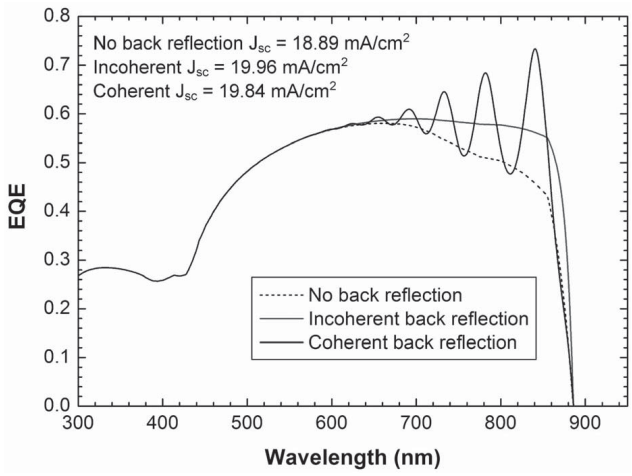

Fig. 3. External quantum efficiency calculated for the GaAs solar cell with no back reflector, incoherent reflection from an Au mirror and coherent reflection from an Au mirror.

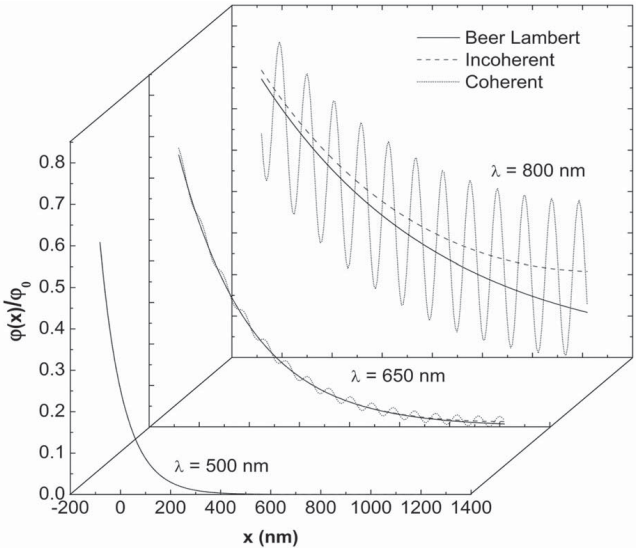

Fig. 4. Relative photon flux in the solar cell for 800 nm wavelength light for the case of no back reflector, incoherent and coherent back reflections.

interference effects are clearly visible in the case of a coherent back reflector.

To further demonstrate the modification of the generation function for the different reflector configurations, Fig. 5 shows the photon flux in the solar cell integrated along the length of the structure as a function of base thickness for 500, 650, and 800 nm light. For the 800 nm light, the interference effects in the cavity lead to large oscillations in the integrated flux with the coherent back reflector. The fringes in the flux are observed for thicknesses corresponding to constructive interference of the forward and reverse propagating fields, with the peak separation given by $\Delta d = n\lambda/2$. At this wavelength, for base thicknesses greater than about 3 microns, the flux in the solar cell becomes approximately equal for the three reflector cases. For thinner solar cells however, the structure with incoherent back reflection has significantly higher flux than with no back reflection. With the coherent back reflector, the peak integrated flux values are significantly larger than

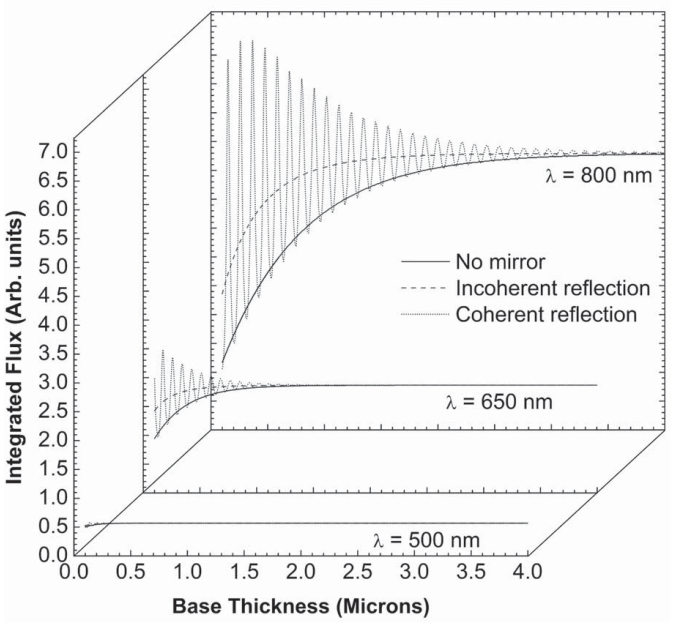

Fig. 5. Integrated flux inside the solar cell at 800 nm for the case of no back reflection, incoherent and coherent back reflections.

the case of incoherent back-reflection, giving large single wavelength improvements in the photocurrent generation for specific solar cell thicknesses. However, it should be noted that over the full spectrum the improvement at these thicknesses is lower than this single wavelength value, as the constructive interference condition is not satisfied over a wider wavelength range.

At 650 nm, the enhancements to the integrated flux are only seen for base thicknesses thinner than approximately 1 micron, as the penetration depth of the light in the structure becomes shorter. Beyond 1 micron, the integrated flux asymptotically approaches a fixed value for all three back reflector conditions when increasing the cell thickness has no impact on the light flux absorbed. In the case of 500 nm light, the short penetration depth of the light means that the integrated flux is relatively independent of the cell thickness, apart from base thicknesses below several hundred nanometers.

VI. Comparison to Experimental Data

To investigate the effectiveness of the model for simulating real solar cell devices, a high efficiency GaAs single junction solar cell was grown by MOCVD and fabricated at MicroLink Devices, Inc. The device uses MicroLink's proprietary epitaxial lift-off technology to remove the substrate and incorporate a thick Ag mirror on the back surface with a 5 Å proprietary adhesion layer. The device design is summarized in Table I.

The full solar cell structure has a significantly more complicated layer structure than the simple np diode simulated thus far. The structure incorporates a window layer, back-surface field layer and a transparent back contact layer. To account for this added complexity, the reflectivity of the front surface in an air ambient, r_1 in Fig. 2, is now the reflectivity of the GaAs and AlInP window combined, calculated using the standard transfer matrix technique. The AlInP optical constants were

TABLE I
SOLAR CELL STRUCTURE GROWN AND FABRICATED AT MICROLINK DEVICES

Layer	Material	Thickness (Å)	Doping (cm^{-3})	SRV (cm/s)
Window	$Al_{0.53}In_{0.47}P$	165	n 1×10^{18}	5×10^{6}
Emitter	GaAs	500	n 2×10^{18}	6.5×10^{4}
Base	GaAs	9100	p 5×10^{17}	5.0×10^{4}
BSF	$In_{0.49}Ga_{0.51}P$	300	p 1×10^{18}	n/a
Transparent back contact	$Al_{0.3}Ga_{0.7}As$	3000	p $> 4 \times 10^{18}$	n/a
Adhesion layer	n/a	5	n/a	n/a
Mirror	Ag	Thick	n/a	n/a

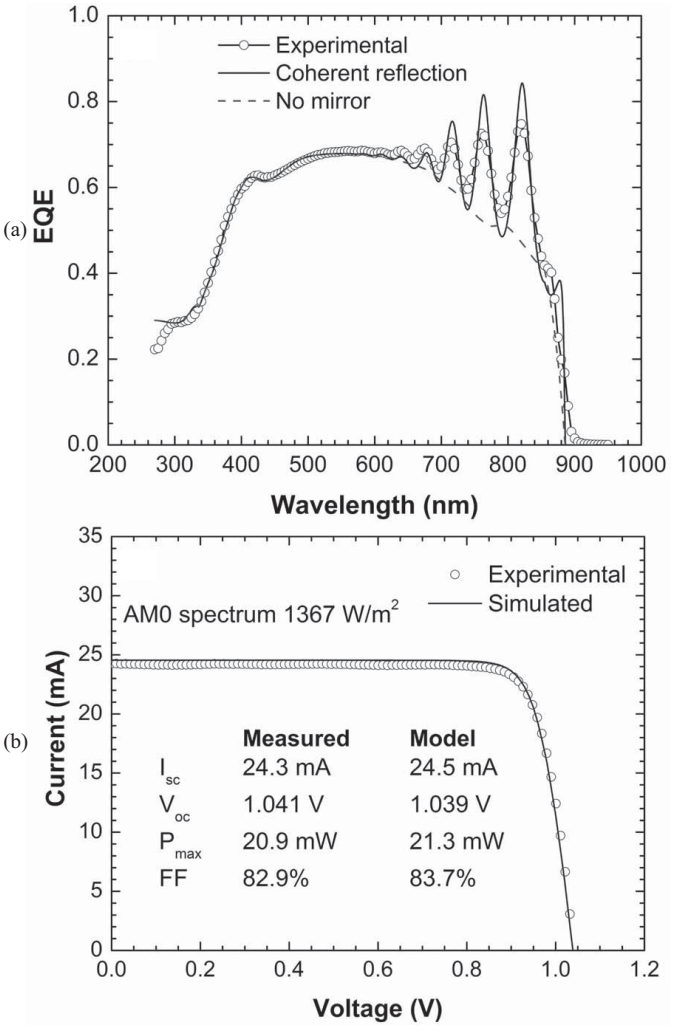

Fig. 6. (a) Measured EQE for the GaAs ELO solar cell with an Ag back mirror (circles), the modeled EQE including coherent reflection (solid line), and no back reflection (dashed line). (b) Measured LIV under the AM0 spectrum, alongside the modeled LIV with coherent back reflection.

taken from a recent publication by Homier *et al*. [25]. The rear surface reflectivity, r_2, is the combined reflectivity of the Ag mirror, adhesion layer, AlGaAs contact layer and BSF layer, in a GaAs ambient. These values of r_1 and r_2 were then used in the equations derived for coherent reflection and used to generate the EQE and IV characteristics of the solar cell. To account for the contribution of the window layer to the EQE, a standard approach described elsewhere [26], [27] was used. This is a good approximation as the window absorbs at short wavelengths, well away from the part of the spectrum where multiple reflections from the back-reflector occur. To account for the absorption in the window, the same argument was used and thus the flux transmitted through the window was attenuated using the Beer–Lambert law. To make the fringes in the EQE clearly visible, no anti-reflection coating was applied to the structure. The surface recombination velocities in the emitter, window and base, were chosen to give the best fit of the calculated EQE curve to the measured data. The SRH lifetimes of both electrons and holes were chosen to be 20 ns.

Fig. 6(a) shows the modeled EQE with and without the coherent back reflector, alongside the measured EQE of the device. The coherent reflection model clearly reproduces the experimental data very accurately. However, the fringes in the EQE are slightly more pronounced in the model than in the data, primarily due to the resolution limit of the spectrometer, but this may also indicate a small amount of incoherent reflection. Fig. 6(b) shows the measured LIV curve of the device under 1-sun AM0 illumination, along with the modeled curve. In the simulation, a series resistance of 2.1 Ω cm^2 was applied to improve the fit to the experimental data. The total device area was 1.108 cm^2 and the exposed area of the device was 0.998 cm^2. The measured and modeled figures of merit for the solar cell are summarized in Fig. 6(b), demonstrating good agreement with theory and experiment. The main sources of uncertainty in these figures of merit arise from the uncertainty in the absolute measurement of EQE and the accuracy of the simulated AM0 spectrum.

VII. CONCLUSION

In this paper we have extended the well-established, 1-D Hovel model to include the effect of both coherent and incoherent back reflection in a homojunction solar cell. A summation approach was used to derive compact analytical generation functions for the two cases and provide a fully consistent analytical solution to the drift-diffusion problem. We have used a simple GaAs np diode as a demonstrative example of the new model and compared the model prediction to data from a real GaAs device fabricated using an ELO technique, incorporating an Ag back reflector. The model was able to accurately reproduce the shape of the EQE curve and accurately predict the figures of merit derived from the LIV curve of the device under 1-sun AM0 illumination. The model is easily extendable to incorporate anti-reflection coatings, and the derivation should serve as a useful tool for device designers

making computationally efficient and realistic calculations for high efficiency device architectures.

ACKNOWLEDGMENT

The authors are extremely grateful to Dr. I. Vurgaftman and Dr. M. González for many helpful discussions and suggestions during in the preparation of this paper. This work was supported by the Office of Naval Research.

REFERENCES

[1] H. J. Hovel and J. M. Woodall, "The effect of depletion region recombination currents on the efficiencies of Si and GaAs solar cells," in *Proc. 10th IEEE Photovolt. Specialist Conf.*, 1973, p. 25.
[2] H. J. Hovel, *Solar Cells*. New York, USA: Academic, 1975.
[3] M. Y. Ghannam, S. El-Naggar, N. Rafat, and A. A. Abouelsaood, "Analytical study of carrier photogeneration and photocurrent in thin silicon solar cells with specular and diffuse back reflection," *IEEE Trans. Electron Devices*, vol. 46, no. 10, pp. 2072–2079, Oct. 1999.
[4] L. A. Hussain, "Back-reflection effect on long-wavelength spectral response of solar-cells," *J. Phys. D, Appl. Phys.*, vol. 11, no. 11, pp. 1535–1537, Aug. 1978.
[5] P. Campbell and M. A. Green, "Light trapping properties of pyramidally textured surfaces," *J. Appl. Phys.*, vol. 62, no. 1, pp. 243–249, Feb. 1987.
[6] R. Brendel, *Thin-Film Crystalline Silicon Solar Cells*. New York, USA: Wiley, 2003.
[7] M. A. Green, "Lambertian light trapping in textured solar cells and light-emitting diodes: Analytical solutions," *Progr. Photovolt. Res. Appl.*, vol. 10, no. 4, pp. 235–241, Apr. 2002.
[8] A. Mellor, I. Tobías, A. Martí, M. J. Mendes, and A. Luque, "Upper limits to absorption enhancement in thick solar cells using diffraction gratings," *Progr. Photovolt. Res. Appl.*, vol. 19, no. 6, pp. 676–687, Sep. 2011.
[9] P. A. Basore, "Numerical modeling of textured silicon solar cells using PC-1D," *IEEE Trans. Electron Devices*, vol. 37, no. 2, pp. 337–343, Feb. 1990.
[10] G. Létay, M. Hermle, and A. W. Bett, "Simulating single-junction GaAs solar cells including photon recycling," *Progr. Photovolt. Res. Appl.*, vol. 14, no. 8, pp. 683–696, Dec. 2006.
[11] Z. Q. Li, Y. G. Xiao, and Z. M. S. Li, "Two-dimensional simulation of GaInP/GaAs/Ge triple junction solar cell," *Phys. Status Solidi C*, vol. 4, no. 5, pp. 1637–1640, Apr. 2007.
[12] R. Stangl, M. Kriegel, and M. Schmidt, "AFORS-HET, version 2.2, a numerical computer program for simulation of heterojunction solar cells and measurements," in *Proc. IEEE 4th World Conf. Photovolt. Energy Convers. Conf. Rec.*, May 2006, pp. 1350–1353.
[13] J.-Y. Chang, S.-H. Yen, Y.-A. Chang, and Y.-K. Kuo, "Simulation of high-efficiency GaN/InGaN p-i-n solar cell with suppressed polarization and barrier effects," *IEEE J. Quantum Electron.*, vol. 49, no. 1, pp. 17–23, Jan. 2013.
[14] O. S. Heavens, *Optical Properties of Thin Solid Films*. London, U.K.: Butterworths, 1955.
[15] B. Harbecke, "Coherent and incoherent reflection and transmission of multilayer structures," *Appl. Phys. B*, vol. 39, no. 3, pp. 165–170, Mar. 1986.
[16] S. J. Fonash, *Solar Cell Device Physics*, 2nd ed. New York, USA: Academic, 2010.
[17] S. Adachi, "Optical constants of crystalline and amorphous semiconductors," in *Numerical and Graphical Information*. Norwell, MA, USA: Kluwer, 1999.
[18] J. S. Blakemore, "Semiconducting and other major properties of gallium arsenide," *J. Appl. Phys.*, vol. 53, no. 10, pp. 123–181, May 1982.
[19] R. N. Hall, "Recombination processes in semiconductors," *Proc. IEE B, Electron. Commun. Eng.*, vol. 106, no. 17, pp. 923–931, May 1959.
[20] G. B. Lush, "B-coefficient in n-type GaAs," *Solar Energy Mater. Solar Cells*, vol. 93, no. 8, pp. 1225–1229, Aug. 2009.
[21] D. C. Johnson, I. M. Ballard, K. W. J. Barnham, J. P. Connolly, M. Mazzer, A. Bessiere, C. Calder, G. Hill, and J. S. Roberts, "Observation of photon recycling in strain-balanced quantum well solar cells," *Appl. Phys. Lett.*, vol. 90, no. 21, pp. 213505-1–213505-3, May 2007.
[22] C. T. Sah, R. N. Noyce, and W. Shockley, "Carrier generation and recombination in p-n junctions and p-n junction characteristics," *Proc. IRE*, vol. 45, no. 9, pp. 1228–1243, Sep. 1957.
[23] J. Nelson, *The Physics of Solar Cells*. London, U.K.: Imperial College Press, 2003.
[24] I. Vurgaftman, J. R. Meyer, and L. R. Ram-Mohan, "Band parameters for III–V compound semiconductors and their alloys," *J. Appl. Phys.*, vol. 89, no. 11, pp. 5815–5875, Feb. 2001.
[25] R. Homier, A. Jaouad, A. Turala, C. E. Valdivia, D. Masson, S. G. Wallace, S. Fafard, R. Ares, and V. Aimez, "Antireflection coating design for triple-junction III–V/Ge high-efficiency solar cells using low absorption PECVD silicon nitride," *IEEE J. Photovolt.*, vol. 2, no. 3, pp. 393–397, Jul. 2012.
[26] X. M. Dai and Y. H. Tang, "A simple general analytical solution for the quantum efficiency of front-surface-field solar cells," *Solar Energy Mater. Solar Cells*, vol. 43, no. 4, pp. 363–376, Oct. 1996.
[27] A. Belghachi and A. Helmaoui, "Effect of the front surface field on GaAs solar cell photocurrent," *Solar Energy Mater. Solar Cells*, vol. 92, no. 6, pp. 667–672, Feb. 2008.

Matthew P. Lumb was born in Halifax, U.K., on April 2, 1983. He received the M.Sc. degree in physics from the University of Durham, Durham, U.K., and the Ph.D. degree from Imperial College London, London, U.K., in 2005 and 2009, respectively.

He was with a start-up company called QuantaSol based in Kingston upon Thames, U.K., from 2009 to 2011. He was the Lead Modeler, developing high efficiency III–V multijunction photovoltaics incorporating strain-balanced quantum wells. In 2011, he then joined the George Washington University, Washington, DC, USA, and the Naval Research Laboratory, Washington DC, modeling multiple aspects of high efficiency photovoltaics, tunnel diodes and optical coatings.

Christopher G. Bailey received the B.S. degree in mechanical engineering from the Rochester Institute of Technology, Rochester, NY, USA, in 2003, and the M.S. degree in materials science engineering from the University of Rochester, Rochester, NY, USA, in 2006, and the Ph.D. degree in microsystems engineering from the Rochester Institute of Technology, Rochester, in 2012.

He joined the U.S. Naval Research Laboratory, Washington, DC, USA, in 2012, as a National Research Council Post-Doctoral Fellow. He is currently beginning his 2nd year in this fellowship. His current research interests include the investigation of material properties and device design of III–V devices, with a specific focus on nanostructured photovoltaic architectures.

Jessica G. J. Adams received the M.Sc. degree in physics and the Ph.D. degree in nano-structured III–V photovoltaics from Imperial College London, London, U.K., in 2006 and 2011, respectively.

She has been working at MicroLink Devices Inc. as a Senior Research and Development Engineer since 2011. Her work involves the development of single-junction and multi-junction solar cells in the GaAs and InP material systems for a range of applications including concentrator photovoltaics systems, space satellites and unmanned aerial vehicles.

Glen Hillier was born in Windsor, ON, Canada, on April 22, 1962. He received the B.Sc. degree in physics from the University of Waterloo, Waterloo, ON, Canada, in 1985.

He was with Bell Northern Research, Ottawa, ON, Canada, from 1985 to 2003 where he was instrumental in developing metal organic vapor phase epitaxy (MOVPE) for use in optical components and high speed electronics. This work included MOVPE development for production of 1.3 to 1.55 micron wavelength laser diodes, detectors and modulators and resulted in the patenting of a novel inverted wafer rotation system for MOVPE. Glen lead the MOVPE team in the development of GaInP based hetero-junction bipolar transistor material that was subsequently used in OC192 optical transmission systems by Nortel Networks. In 2004, he joined MicroLink Devices where he performed the first 100 mm diameter epitaxial lift-off of GaAs and InP based materials. This work included the development of inverted metamorphic junction solar cells on GaAs and dual junction solar cells on InP. He continues work developing InP and GaAs based materials for optical and electronic devices.

Francis Tuminello received the B.S. degree in physics from the University of Illinois, Chicago, IL, USA, in 2000.

He has worked in both III–V molecular beam expitaxy and single crystal sapphire growth. He has been a Process Engineer with Microlink Devices, Niles, IL, USA, since 2008.

Victor C. Elarde received the Ph.D. degree in electrical engineering from the University of Illinois, Urbana-Champaign, Urbana, IL, USA, in 2007.

He was a Research and Development Engineer with QPC Lasers, Inc. Los Angeles, CA, USA, where he worked on high-power semiconductor lasers for medical, industrial, and display applications. In 2009, he joined MicroLink Devices, Niles, IL, USA, as a Research and a Development Engineer and is currently working on multi-junction III–V solar cell devices. This work is primarily focused on improving the efficiency of inverted, metamorphic, triplejunction devices for both one-sun and concentrator applications. He is experienced in all areas of solar cell development and characterization including epitaxial structure engineering, fabrication process development, anti-reflection coating design and deposition, packaging and thermal design, quantum efficiency measurement and analysis, and LIV characterization. He is also experienced in numerical modeling as applied to semiconductor, optical, and quantum systems.

Robert J. Walters received the B.S. degree in physics in 1988 from Loyola College, Baltimore, MD, USA, and the M.S. and Ph.D. degrees in applied physics from the University of Maryland, in 1990 and 1994, respectively.

He is a Research Physicist with the Naval Research Laboratory (NRL), Washington, DC, USA, and the Head of the Solid State Devices Branch. He has been with NRL since 1990, and he is currently a Head of the Solid State Devices Branch. The research within his Branch includes radiation effects in spacecraft electronics, advanced detectors ranging from the UV to the SWIR, MWIR, LWIR, and VLWIR, photovoltaics, and space technology demonstration experiments.